Flux-tunable parity-protected qubit based on a single full-shell nanowire Josephson junction

G. Giavaras,* Rubén Seoane Souto, Maria José Calderón, and Ramón Aguado†
Instituto de Ciencia de Materiales de Madrid (ICMM), Consejo Superior de Investigaciones Científicas (CSIC), Sor Juana Inés de la Cruz 3, 28049 Madrid, Spain

(Received 7 March 2025; accepted 29 May 2025; published 16 June 2025)

Leveraging the higher harmonics content of the Josephson potential in a superconducting circuit offers a promising route in the search for new qubits with increased protection against decoherence. In this work, we demonstrate how the flux tunability of a hybrid semiconductor-superconductor Josephson junction based on a single full-shell nanowire enables this possibility. Near one flux quantum, $\Phi \approx \Phi_0 = h/2e$, we find that the qubit system can be tuned from a gatemon regime to a parity-protected regime with qubit eigenstates localized in phase space in the $\varphi_0 = 0$ and π minima of the Josephson potential ($\cos 2\varphi_0$). Estimates of qubit coherence and relaxation times due to different noise sources are presented.

DOI: 10.1103/6kxs-wnbw

I. INTRODUCTION

The coupling of a physical qubit to its noisy environment inevitably causes relaxation and dephasing, which is one of the main obstacles in the practical development of a scalable quantum computer [1]. In addition to quantum error correction [2], an interesting approach is to engineer intrinsic noise protection by designing the underlying qubit Hamiltonian and achieving computational states that are largely decoupled from local noise channels [3].

Among the various approaches for noise protection, a powerful idea is to encode qubits in global degrees of freedom that are insensitive to local fluctuations, which is the main idea behind topological qubits [4,5]. Another interesting approach is to encode qubits in local decoherence-free subspaces, based on effective Hamiltonians with parity symmetry [6,7]. Although partial noise protection is possible in superconducting circuits based on a single quantum degree of freedom, full protection in both the relaxation (T_1) and dephasing (T_2) channels is challenging, and usually complex multimode circuits are needed [8,9].

Given the above context, it is important to design simple circuits to realize parity-protected qubits [7,10–13]. A basic advantage of the parity protection is that relaxation due to charge-induced noise can be suppressed leading to an enhanced T_1 time. In hybrid superconductor-semiconductor Josephson junctions important steps have been taken towards the realization of parity-protected qubits by leveraging the higher harmonics content of the Josephson potential[1]

$$V_J(\varphi_0) = \sum_{M \geqslant 1} E_{J,M} \cos(M\varphi_0), \tag{1}$$

with φ_0 being the superconducting phase difference and $E_{J,M}$ the Fourier components. Here the key observation is that control of $E_{J,M}$, for example using electrostatic gates, can result in a double-well (DW) Josephson potential $V_J(\varphi_0) = E_{J,2}\cos(2\varphi_0)$, which is needed to define a parity-protected qubit [10,14,15]. Because the qubit eigenstates of the DW Josephson potential are also eigenstates of the Cooper-pair parity operator the charge-induced noise in a superconducting qubit circuit can be suppressed.

An interferometer formed by two Josephson junctions, gate-tuned into balance and frustrated by a half-quantum of magnetic flux, yields a $\cos 2\varphi_0$ Josephson element [12,16–22]. This scheme has been successfully incorporated into a superconducting circuit to demonstrate parity-protected regimes characterized by an enhanced T_1 time [14]. More complex geometries involving four Josephson junctions have also been explored, and the resulting Josephson potential has been precisely tuned with a combination of gates and magnetic frustration [23].

In the present work we theoretically explore the possibility of tuning the higher harmonics content in a *single* Josephson junction and creating a DW Josephson potential. Our proposal is based on the flux tunability of a Josephson junction formed in a full-shell nanowire (NW) [24]. Although some experiments have explored qubits in full-shell NWs [25–27], there is no theoretical work that investigates the influence of the full-shell geometry on the qubit properties and, in particular, the possibility of obtaining parity-protected regimes. Importantly, we show that the Josephson potential can be tuned with an applied magnetic flux, Φ, threading the NW cross section, and specifically demonstrate realistic regimes where the Josephson potential changes from a single well (SW), with a minimum located at $\varphi_0 = 0$, to a DW with minima at $\varphi_0 = 0$ and $\varphi_0 = \pi$.

Our study shows that the flux tunability can be accomplished inside the so-called first Little-Parks (LP) lobe around $\Phi \approx \Phi_0 = h/2e$ [28–31]. The strongest SW potential is formed at the center of the LP lobe ($\Phi = \Phi_0$), and the DW is formed at two flux values located symmetrically around

*Contact author: g.giavaras@gmail.com
†Contact author: ramon.aguado@csic.es

[1]We neglect Fourier terms $E'_{J,M}\sin(M\varphi_0)$ which are nonzero only when both time-reversal and inversion symmetries are broken. They could be incorporated in our analysis in such symmetry-broken situations.

$\Phi = \Phi_0$. The SW potential can define a usual gate-tunable transmon qubit (gatemon), whereas the DW can define a $\cos 2\varphi_0$ parity-protected qubit. We also present estimates of both T_1 and T_2 times due to various noise channels and find coherence times similar to those measured in experiments [14]. Our overall analysis suggests that control and readout of a full-shell NW parity-protected qubit should be feasible.

The paper is organized as follows: In Sec. II we present the model of the Josephson junction formed in a full-shell NW. In Sec. III we study how the applied magnetic flux can be used to tune the Josephson potential and give rise to different regimes. In the same section we employ a simplified junction model based on approximate expressions for the Andreev bound states (ABSs). This model provides valuable insight into the flux dependence of the exact Josephson potential. The coherence properties of the resulting qubits are examined in Sec. IV, and finally the conclusions of our work are summarized in Sec. V. Some more technical parts are presented in the Appendixes. The Bogoliubov-de-Gennes (BdG) Hamiltonian of the full-shell NW is detailed in Appendix A, while the flux modulation of the pairing potential due to the LP effect is described in Appendix B. Additional examples of the Josephson potential, including deviations from the perfect cylindrical symmetry, are presented in Appendix C. In Appendix D we investigate the Josephson potential with spin-orbit coupling and show that beyond the DW a triple-well potential can also arise in the topological regime due to the appearance of Majorana states. In Appendix E we present various approximate results derived from a simplified junction model. Finally, in Appendix F the coherence times of the parity protected qubit are further explored and an approximate model is presented to extract the qubit levels.

II. FULL-SHELL NANOWIRE JOSEPHSON JUNCTION

A. Full-shell nanowire Hamiltonian

Full-shell hybrid NWs are semiconducting NWs fully wrapped by a thin superconducting shell, as shown in Fig. 1(a). We consider the hollow-core approximation which assumes that the electrons are confined near the surface of the NW. As detailed in Appendix A, without spin-orbit coupling the BdG Hamiltonian describing the proximitized NW consists of the two matrices

$$H^{\pm} = \begin{pmatrix} \frac{p_z^2}{2m^*} + \mu_e^{\pm} & \Delta \\ \Delta^* & -\frac{p_z^2}{2m^*} + \mu_h^{\pm} \end{pmatrix}, \tag{2}$$

where $p_z = -i\hbar\partial_z$ is the momentum operator along the NW, Δ is the superconducting pairing potential, and m^* is the effective mass of the NW.

An applied magnetic flux Φ through the cross-section of the NW causes the superconducting phase in the shell to acquire a quantized winding number n (also called fluxoid) around the NW axis. Defining the normalized flux $n_\Phi = \Phi/\Phi_0$, with $\Phi_0 = h/2e$, the winding number reads $n = \lfloor n_\Phi \rceil$, and deviations from integer fluxes are measured through the variable

$$\phi = n - n_\Phi = n - \frac{\Phi}{\Phi_0}. \tag{3}$$

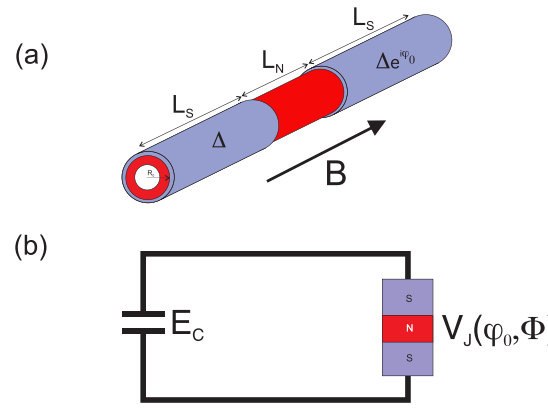

FIG. 1. (a) Schematic illustration of a full-shell NW Josephson junction. A semiconducting core (red) of radius R_0 is wrapped by a superconducting shell (mauve) of negligible thickness. A middle unwrapped region defines a superconducting-normal-superconducting (SNS) Josephson junction: two S regions of length L_S are separated by a N region of length L_N, where Δ is the pairing potential and φ_0 is the superconducting phase difference. In the hollow-core approximation the electrons are confined near the surface of the NW, and under an applied axial magnetic field B the NW is threaded by a magnetic flux $\Phi = \pi R_0^2 B$. (b) Superconducting qubit circuit where the Josephson element is the SNS junction in panel (a). The circuit consists of a capacitor with a charging energy E_c, and a flux-dependent Josephson potential $V_J(\varphi_0, \Phi)$ whose Fourier decomposition contains higher harmonics, Eq. (7).

Tuning Φ results in winding jumps accompanied by a repeated suppression and recovery of the superconducting pairing potential, $\Delta = \Delta(\Phi)$ (Appendix B). These jumps form the so-called LP lobes[2] associated with each n, with $\phi = 0$ corresponding to the middle of the lobe [32]. While in realistic configurations the LP effect is always present, when the coherence length ξ of the superconducting shell is much smaller than the radius R_0 of the NW the pairing potential is approximately flux independent, $\Delta(\Phi) \approx \Delta(0) = \Delta_0$. In the present work, we study the physics of the Josephson junction in the first LP lobe, namely, $n = 1$ and $0.5 \leqslant \Phi/\Phi_0 \leqslant 1.5$.

For a NW of radius R_0 the BdG energy levels are characterized by the angular-momentum number m_j, and the flux-dependent chemical potentials which, without spin-orbit coupling, can be written as [24,33]

$$\mu_e^{\pm}(\phi) = -\mu + \frac{\hbar^2}{8m^* R_0^2}(1 \mp 2m_j \pm \phi)^2, \tag{4}$$

where μ is the flux-independent chemical potential of the NW. Similar chemical potentials, $\mu_h^{\pm}(\phi)$, can be defined for the holes (Appendix A). Due to these effective chemical potentials the BdG energy levels shift with flux, and near the center

[2]Essentially the same mechanism underlies the LP effect, a modulation of the transition temperature, T_c, of a superconducting cylinder with magnetic flux leading to a reentrant destruction of superconductivity near odd half-integer multiples of Φ_0 [28–31].

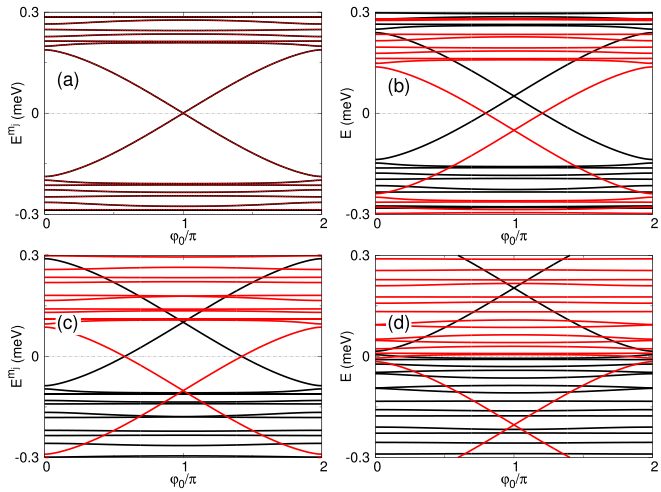

FIG. 2. BdG energy levels E^{m_j} for $m_j = 1$ and $m_j = -1$ as a function of superconducting phase at different fluxes: (a) $\Phi/\Phi_0 = 1$, (b) 1.1, (c) 1.2, and (d) 1.4. $E^{-1} = -E^1$ due to electron-hole symmetry. Parameters: $L_S = 2000$ nm, $L_N = 100$ nm, $R_0 = 50$ nm, and $\Delta = \Delta_0 = 0.2$ meV.

of a lobe this shift is approximately linear

$$\mu_e^{\pm}(\phi) \approx \pm\frac{\hbar^2}{4m^*R_0^2}(1 \mp 2m_j)\phi. \tag{5}$$

The first term (m_j independent) can be interpreted as a Zeeman-like contribution and the second one has an orbital origin describing the coupling between the magnetic field and the angular momentum [24,33,34]. Away from the lobe's center the quadratic ϕ^2 corrections start to play a role.

B. Defining the Josephson potential

The Josephson junction shown in Fig. 1(a) consists of a normal (N) region of length L_N between two full-shell hybrid NWs defining two superconducting (S) regions of length L_S. In the N region the pairing potential is zero while in the left and right S regions the pairing potentials are equal to Δ and $\Delta e^{i\varphi_0}$, respectively, with φ_0 being the superconducting phase difference. The Josephson potential $V_J(\varphi_0)$ is calculated from the free energy of the Josephson junction, thus in the limit of zero temperature $V_J(\varphi_0)$ can be written as the sum of different angular momenta m_j contributions

$$V_J(\varphi_0) = \sum_{m_j} V_J^{m_j}(\varphi_0) = \sum_{m_j}\sum_{k<0} E_k^{m_j}(\varphi_0). \tag{6}$$

Here, $E_k^{m_j}$ denotes the eigenenergies of the Josephson junction that correspond to m_j and for each φ_0 we sum the eigenenergies below zero ($k < 0$) until $V_J^{m_j}(\varphi_0)$ converges. This means we only need to consider $E_k^{m_j}$ with a significant φ_0 dispersion. The eigenenergies in Eq. (6) are obtained from the numerical solution of the BdG Hamiltonian, Eq. (2).

Figure 2 illustrates a representative example of the BdG energy levels $E_k^{m_j}$ at different fluxes. Increasing the magnetic flux shifts the $m_j = 1$ levels upwards and eventually the subgap mode crosses zero energy, Fig. 2(d). The corresponding $m_j = -1$ levels shift downwards and satisfy $E_k^{-1} = -E_k^1$, thus the zero-energy crossing leads to a so-called 0-π transition where positive and negative BdG levels are exchanged. The flux-induced shift of the BdG levels can be understood from the linear ϕ term in Eq. (5). Near the center of a lobe this term has the dominant role, whereas away from the center the quadratic ϕ^2 term is also significant and the flux dependence of the BdG levels is more complicated.[3] Away from the lobe's center the Josephson potential can drastically change compared with that at $\Phi/\Phi_0 = 1$ provided the flux-induced shift of the Andreev levels is large. This remark indicates that a nanowire with a smaller radius is advantageous to induce a larger shift and produce a DW potential.

In the next sections, it is helpful to look at the flux dependence of the Josephson potential. For this reason we combine Eqs. (1) and (6), and we now explicitly denote the flux dependence in the BdG energy levels and Fourier decomposition:

$$V_J(\varphi_0, \Phi) = \sum_{m_j}\sum_{k<0} E_k^{m_j}(\varphi_0, \Phi) = \sum_{M\geqslant 1} E_{J,M}(\Phi)\cos(M\varphi_0). \tag{7}$$

In Sec. III we determine the flux dependence of $E_{J,M}(\Phi)$ for different junctions and demonstrate how the applied magnetic flux can tune the Josephson potential from a SW to a DW.

III. FROM SINGLE- TO DOUBLE-WELL REGIME

A. Examples of Josephson potentials

In this section we present some characteristic examples of the Josephson potential while additional results as well as a brief investigation about the role of deviations from the perfect cylindrical symmetry can be found in Appendix C. To simplify the presentation we focus on low chemical potentials μ so that only the $m_j = 0, \pm 1$ modes contribute to the Josephson potential. Including additional m_j modes only affects the quantitative properties of the DW. We consider a junction without spin-orbit coupling, $\alpha_{so} = 0$, which leads to degenerate BdG levels [33], and explore the $\alpha_{so} \neq 0$ case in Appendix D. We also assume the thickness of the superconducting shell to be much smaller than the radius of the NW. Under this assumption the flux modulation of the pairing potential due to the LP effect is symmetric with respect to the center of the lobe, $\Phi/\Phi_0 = 1$. Finally, we consider the chemical potential μ to be the same in the S and N regions. This choice reduces the number of parameters, but does not affect the main conclusions. In a more realistic configuration the number of modes in the junction can be adjusted by tuning the chemical potential within the N region [33].

The first few Fourier components of the Josephson potential as a function of the magnetic flux are shown in Fig. 3(a). Figures 3(b)–3(e) show the resulting Josephson potentials at different fluxes. At the center of the LP lobe, $\Phi/\Phi_0 = 1$, the component $E_{J,1}$ dominates giving rise to a SW Josephson

[3]See Ref. [33] for a detailed description of the flux dependence of the BdG spectrum and the resulting flux-tunable critical current within the hollow-core model. More advanced numerical simulations are presented in Ref. [35].

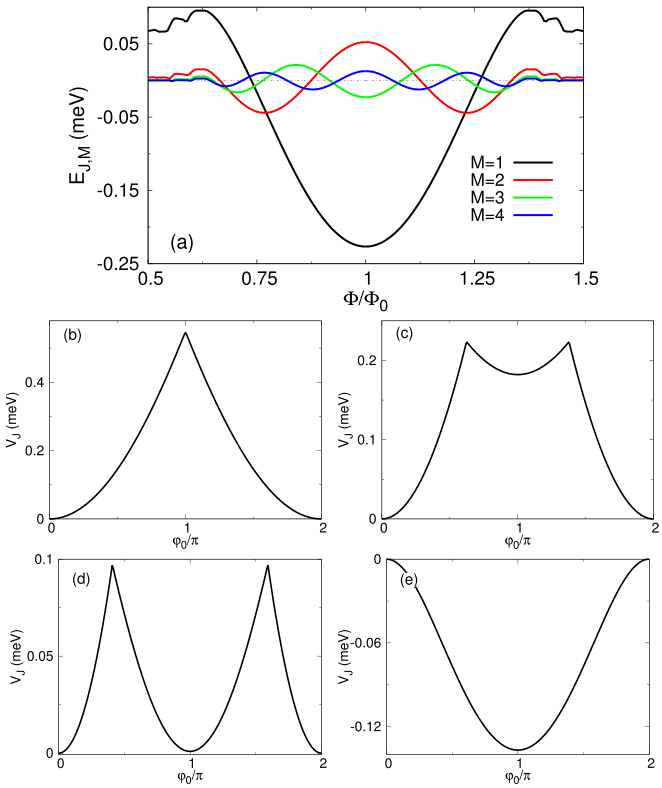

FIG. 3. (a) Fourier components of the Josephson potential for $M = 1$–4 as a function of magnetic flux. Josephson potential at different fluxes: (b) $\Phi/\Phi_0 = 1$, (c) 1.18, (d) 1.26, and (e) 1.5. Parameters: $L_S = 2000$ nm, $L_N = 100$ nm, $R_0 = 50$ nm, and $\Delta = \Delta_0 = 0.2$ meV.

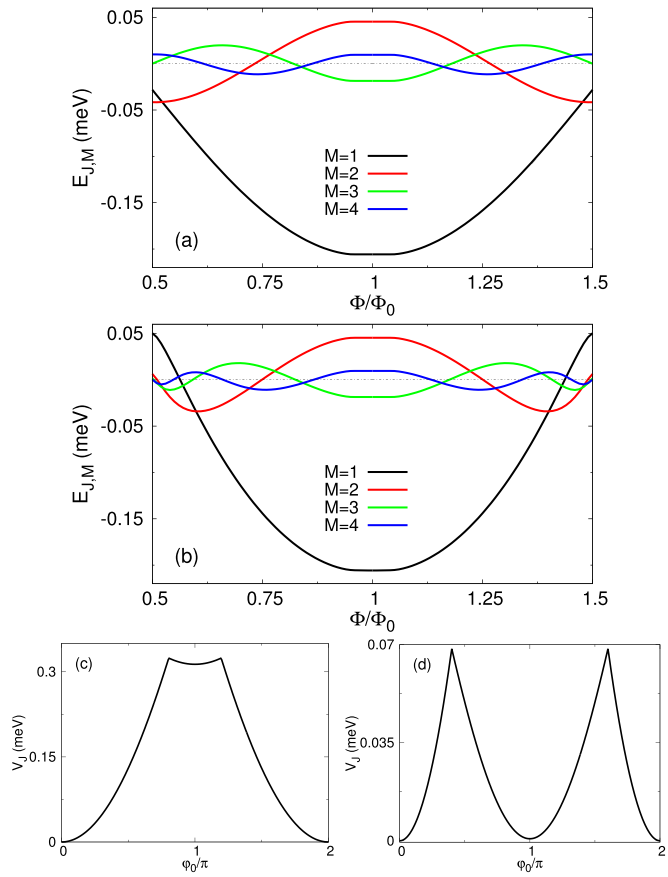

FIG. 4. (a) Fourier components of the Josephson potential for $M = 1$–4 as a function of magnetic flux for a constant $\Delta = \Delta_0 = 0.2$ meV. (b) As in panel (a) but for a flux-dependent $\Delta = \Delta(\Phi)$, and $\xi = 110$ nm. Josephson potential for $\Delta = \Delta(\Phi)$, and $\xi = 110$ nm at different fluxes: (c) $\Phi/\Phi_0 = 1.2$, and (d) 1.44. Parameters: $L_S = 2000$ nm, $L_N = 100$ nm, and $R_0 = 75$ nm.

potential. By tuning the flux away from $\Phi/\Phi_0 = 1$ the $E_{J,1}$ component decreases and $E_{J,2}$ becomes the dominant one, with $E_{J,1} \approx 0$ at $\Phi/\Phi_0 \approx 1.26$ and 0.74. At these fluxes, a DW potential with equal minima $V_J(\varphi_0 = 0) \approx V_J(\varphi_0 = \pi)$ is formed, Fig. 3(d). This condition entails the sum of the odd Fourier components to be nearly zero. We refer to this DW potential as *symmetric*, although the two well widths differ because in general $E_{J,M} \neq 0$ for $M \neq 2$. In Sec. IV we show that for a symmetric DW a quasidegenerate parity-protected qubit can be defined. Notice that Figs. 3(b) and 3(e) reveal that the Josephson potential undergoes a 0-π transition, characterized by the shift of the SW potential from $\varphi_0 = 0$ to π. We emphasize that this transition depends sensitively on the exact junction parameters, but is not required to define a symmetric DW potential.

In full-shell NWs the LP effect leads to a flux-dependent pairing potential, $\Delta = \Delta(\Phi)$ (Appendix B). The coherence length ξ of the superconducting shell, as well as the radius R_0 of the NW, determines the strength of the flux dependence. DWs formed near the center of a lobe are weakly affected by the flux dependence of Δ and our numerical investigation in Appendix C demonstrates that the DW in Fig. 3(d) remains to a very good approximation unaffected by the LP effect when $\xi \approx 120$ nm (destructive regime) or smaller.

Although the SW potential at a lobe's center can be found in any junction, the formation of a symmetric DW is not guaranteed. One such case is illustrated in Fig. 4(a) for a NW with $R_0 = 75$ nm. Now $E_{J,1}$ is large within the entire LP lobe, consequently, only highly asymmetric DWs are formed. However, when we take into account the flux dependence of the pairing potential [Fig. 4(b)] a symmetric DW is formed at $\Phi/\Phi_0 \approx 1.44$ and 0.56 [Fig. 4(d)]. This behavior is general for NWs with $R_0 \gtrsim 70$–80 nm and suitable values of the coherence length ξ. A numerical example in Appendix E demonstrates that a larger ξ is needed to form a DW potential as R_0 increases.

Finally, we comment on the junction length L_N. We have studied junctions for different paraments and found that, in general, longer junctions are more appropriate to define a DW potential. Increasing L_N shifts the DW regime closer to the center of the LP lobe, because the φ_0 dispersion of the energy levels lying above the superconducting gap becomes stronger. We present a characteristic example in Appendix C comparing two junctions with $L_N = 100$ nm and 200 nm. Tuning the magnetic flux forms a DW only for the longer junction.

B. Simplified Josephson junction

The results in Figs. 3 and 4 can be understood from the flux dependence of the ABSs levels lying in the superconducting

gap as well as the energy levels lying above the gap. The latter are important to form the DW potential, provided their overall φ_0 dispersion is opposite to that of the ABSs subgap levels. To overcome the difficulties due to the complexity of the BdG Hamiltonian, we here develop a simplified model. Specifically, we assume for $m_j = 1$ the ABS subgap level,

$$E_{\pm,s}(\varphi_0, \Phi) = \pm\Delta(\Phi)\sqrt{1 - \tau_s \sin^2(\varphi_0/2)} + \gamma(\Phi), \quad (8)$$

where $0 < \tau_s \leqslant 1$ models the transparency of the Josephson junction, and the term

$$\gamma(\Phi) = -\left(1 - \frac{\Phi}{\Phi_0}\right)\frac{\hbar^2}{4m^* R_0^2}, \quad (9)$$

captures the linear shift due to the applied magnetic flux. For $\gamma(\Phi) = 0$ we recover the standard short-junction formula [36]. We also consider a level which lies above the gap

$$E_{\pm,a}(\varphi_0, \Phi) = \pm\Delta(\Phi)\sqrt{1 - \tau_a \sin^2(\varphi_0/2)} + \gamma(\Phi) \mp \beta. \quad (10)$$

The exact value of the flux independent constant β is not important and we take $\beta \gtrsim 2\Delta_0$ to satisfy the usual regime $E_{+,a} < E_{-,s}$. The levels $E_{-,s}$ and $E_{+,a}$ have opposite φ_0 dispersions and we take the limit $\tau_a < \tau_s$ which models the most usual case in a Josephson junction. The role of $E_{\pm,a}$ is to capture all the levels lying above the gap in the corresponding BdG calculation and have opposite φ_0 dispersion with respect to $E_{\mp,s}$.

Within the simplified model analytical conditions can be derived and some simple limits can be identified. Using the definition, Eq. (7), and with the BdG levels $E_k^{m_j}(\varphi_0, \Phi)$ being $E_{\pm,a}(\varphi_0, \Phi)$ and $E_{\pm,s}(\varphi_0, \Phi)$ we can show that at $\Phi/\Phi_0 = 1$ the Josephson potential has a single minimum at $\varphi_0 = 0$. By increasing Φ the Fourier coefficients vary with flux (Appendix E) in the same way as in Fig. 4(b), thus the shape of the potential can drastically change. Equation (7) suggests that only when $E_{-s}(\pi, \Phi) > 0$ the applied magnetic flux starts to modify the SW potential. Therefore, away from the lobe's center the required Φ to observe a change in the Josephson potential satisfies $\gamma(\Phi)/\Delta(\Phi) > \sqrt{1 - \tau_s}$. By further increasing Φ, the necessary condition leading to a symmetric DW potential is

$$E_{+,a}(\pi, \Phi) = E_{+,a}(0, \Phi) + E_{-,s}(0, \Phi), \quad (11)$$

which guarantees that the Josephson potential has equal minima at $\varphi_0 = 0$ and π. Equation (11) reveals the significance of the level $E_{\pm,a}$; if this is not taken into account Eq. (11) cannot be satisfied. This can be be understood by taking the tunneling limit $\tau_a \to 0$ that leads to a nondispersive level $E_{+,a}$. The flux $\Phi = \Phi_{\rm DW}$ satisfying Eq. (11) is given by the expression

$$\frac{\gamma(\Phi_{\rm DW})}{\Delta(\Phi_{\rm DW})} = \sqrt{1 - \tau_a}. \quad (12)$$

Because $\tau_a < 1$ Eq. (12) imposes the constraint $\gamma(\Phi_{\rm DW}) < \Delta(\Phi_{\rm DW})$, and simultaneously the junction parameters need to be controlled so that $\Phi_{\rm DW}$ lies within the first LP lobe. To obtain a physically acceptable $\Phi_{\rm DW}$ a NW with a smaller radius R_0 is advantageous and a longer junction is also preferable since a larger τ_a is expected. Interestingly, the formation of the DW potential does not necessarily require a highly transparent junction. This can be understood from the fact that τ_s is not explicitly involved in Eq. (12). However, a higher τ_s can be advantageous to induce stronger DW potential barriers and thus reduce the qubit frequency.

A more detailed analysis of the simplified model, together with numerical examples, is given in Appendix E. The key point in our analysis is to derive the condition which the junction needs to satisfy in order to form a DW potential. This condition is given by Eqs. (11) and (12). Provided these two equations are satisfied the SW at $\Phi = \Phi_0$ is transformed to a DW at $\Phi = \Phi_{\rm DW}$.

IV. FLUX TUNABLE PARITY-PROTECTED QUBIT

A. General formalism

We now explore our proposed qubit system based on the superconducting circuit schematically shown in Fig. 1(b). The qubit Hamiltonian consists of the charging energy as well as the Josephson potential energy,

$$H = 4E_c(\hat{N} - N_g)^2 + V_J(\hat{\varphi}_0, \Phi), \quad (13)$$

where $\hat{N}$ is the Cooper-pair number operator that is conjugate to $\hat{\varphi}_0$, E_c is the charging energy, and N_g is an offset charge. In the Cooper-pair number basis $|N\rangle$ the Hamiltonian has the form

$$H = \sum_N 4E_c(N - N_g)^2 |N\rangle\langle N| + \sum_{N,M} \frac{1}{2} E_{J,M}(\Phi)|N\rangle\langle N + M| + \text{H.c.}, \quad (14)$$

where the flux-dependent coefficients $E_{J,M}$ are defined in Eq. (7) and $N = 0, \pm 1, \ldots$, is the number of (excess) Cooper pairs. The two lowest eigenstates of this Hamiltonian define the qubit states $|\psi_0\rangle$ and $|\psi_1\rangle$ which are flux-tunable due to the flux dependence of $E_{J,M}$.

We calculate the relaxation times T_1^x due to different noise channels x, from the corresponding rates Γ_1^x derived from the golden rule

$$\frac{1}{T_1^x} = \Gamma_1^x = \frac{1}{\hbar^2}\left|\left\langle \psi_0 \left| \frac{\partial H}{\partial x} \right| \psi_1 \right\rangle\right|^2 S_x(\omega_{10}), \quad (15)$$

where $S_x(\omega_{10})$ is the spectral density at the qubit frequency $\omega_{10} = (E_1 - E_0)/\hbar$. In our qubit system x represents either the magnetic flux, $x = \Phi$, or the charge offset, $x = N_g$, or the chemical potential, $x = \mu$, and at low frequencies a $1/f$ noise is expected

$$S_x(\omega_{10}) = A_x^2\left(\frac{2\pi}{\omega_{10}}\right) \times 1\ \text{Hz}. \quad (16)$$

In superconducting qubits the noise amplitudes A_x can vary by orders of magnitude. The precise values of these amplitudes for qubits based on full-shell NWs are unknown, therefore we take some typical values from the superconducting literature [37,38]: $A_\Phi^2 = (10^{-6}\Phi_0)^2\ \text{Hz}^{-1}$ and $A_{N_g}^2 = (10^{-4}e)^2\ \text{Hz}^{-1}$.

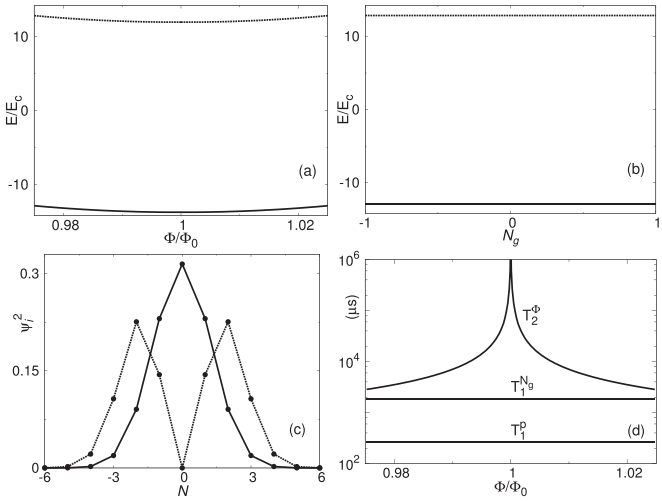

FIG. 5. (a) Energy levels of gatemon qubit (single well) as a function of magnetic flux near the lobe's center. (b) Qubit levels as a function of N_g at $\Phi/\Phi_0 = 1$. (c) Distributions of qubit states at $\Phi/\Phi_0 = 1$. (d) Limiting timescales due to N_g ($T_1^{N_g}$) and Φ (T_2^{Φ}) fluctuations, and quasiparticle relaxation (T_1^p). In all panels $E_c = 0.35$ GHz and $N_g = 0$ unless otherwise stated. For clarity in panels (a) and (b) the energies are shifted near $E = 0$.

Quasiparticle poisoning can also lead to relaxation and the relevant time is derived from the expression [39]

$$\frac{1}{T_1^p} = \Gamma_1^p = |\langle\psi_0|\sin(\hat{\varphi}_0/2)|\psi_1\rangle|^2 S_p(\omega_{10}), \tag{17}$$

with the spectral density given by

$$S_p(\omega_{10}) = \frac{\omega_{10} g_T}{2\pi g_K}\left(\frac{2\Delta}{\hbar\omega_{10}}\right)^{3/2}\chi_p. \tag{18}$$

Here, χ_p is the quasiparticle density normalized to the Cooper-pair density, and we assume the value $\chi_p = 10^{-7}$. The parameters g_K and g_T correspond to the conductance quantum and the junction conductance, respectively [39].

Within a density-matrix approach we can calculate the dephasing time T_2^x of the qubit from the expression [40]

$$T_2^x = \left[2D_x^2 A_x^2 |\ln(\omega_{ir} t)| + 2D_{xx}^2 A_x^4 \kappa\right]^{-1/2}, \tag{19}$$

with $D_x = \partial\omega_{10}/\partial x$, $D_{xx} = \partial^2\omega_{10}/\partial x^2$ and

$$\kappa = \ln^2\left(\frac{\omega_{uv}}{\omega_{ir}}\right) + 2\ln^2(\omega_{ir} t). \tag{20}$$

We assume a measurement timescale of $t = 10$ μs and for $T \lesssim 15$ mK the low- and high-frequency cutoff values of the noise are $\omega_{ir}/2\pi \approx 1$ Hz and $\omega_{uv}/2\pi \approx 3$ GHz, respectively.

B. Qubit properties

For all the calculations in this section we choose the Josephson junction studied in Fig. 3 and explore the qubit properties at different fluxes in the SW and DW regimes. Figure 5 summarizes the results in the SW regime. Near the lobe's center the Josephson potential changes slightly with Φ, hence, the flux dependence of the qubit levels E_0 and E_1 is very weak, Fig. 5(a). In particular, in the limit $\Phi/\Phi_0 \to 1$ the qubit frequency remains to a good approximation constant and the dephasing time T_2^{Φ} is of the order of seconds. The exact value of T_2^{Φ} at $\Phi/\Phi_0 = 1$ cannot be precisely resolved due to numerical round off errors producing spurious derivatives D_{Φ} and $D_{\Phi\Phi}$; therefore, we have introduced a cutoff value of one second. Away from the lobe's center, D_{Φ} increases producing a shorter T_2^{Φ}. In the limit $E_{J,1} \gg E_c$, the qubit levels are only weakly dependent on N_g [38], Fig. 5(b), making the qubit immune to charge dephasing. In Fig. 5(d) we derive T_2^{Φ} based on fluctuations in the applied magnetic flux at a fixed chemical potential. We can also consider dephasing due to fluctuations in the chemical potential. These fluctuations might be the result of disorder along the NW. We assume that $A_{\mu} \sim A_{\Phi}$ and find $T_2^{\mu} \approx 35$ μs ($< T_2^{\Phi}$) at the lobe's center. Thus, this is the limiting dephasing time for the gatemon qubit.

At the lobe's center the gatemon qubit is expected to be linearly insensitive to relaxation due to flux-induced noise because $\partial E_{J,M}/\partial\Phi = 0$, Fig. 3(a). For $N_g = 0$ this property is also valid away from the lobe's center, although in general $\partial E_{J,M}/\partial\Phi \neq 0$. This can be understood from the symmetries of the qubit states $|\psi_0(N)\rangle = |\psi_0(-N)\rangle$ and $|\psi_1(N)\rangle = -|\psi_1(-N)\rangle$. Consequently, the relevant limiting relaxation times for the gatemon qubit are $T_1^{N_g}$ and T_1^p, plotted in Fig. 5(d). We have confirmed that the results in Fig. 5 are general and in the regime $E_{J,1} \gg E_c$ apply equally well to NWs with different radii.

Our above estimates using standard superconducting qubit parameters exceed by more than two orders of magnitude the short relaxation times measured in gatemon qubits based on full-shell NW junctions, $T_1 \approx 0.5$–1 μs, in the first lobe [25]. While the microscopic origin of such short relaxation times is still unclear, subsequent experiments [27] have measured parity lifetimes of the order of 100 ms at $\Phi = 0$. These are consistent with low quasiparticle poisoning and far from limiting the coherence time of the qubit. In the first lobe, however, quasiparticle poisoning is rapidly enhanced, possibly due to the increased density of subgap states (see also Ref. [41]), which may explain the short T_1^p.

Figure 6 summarizes the results in the DW regime. The qubit levels E_0 and E_1 form an anticrossing as a function of the magnetic flux with an energy gap proportional to E_c (Appendix F). Hence, small charging energies lead to a quasidegenerate qubit. From a slightly different point of view, this two-level system essentially operates as a flux qubit with the charging energy governing the tunneling term between the minima. At temperatures $T \lesssim 15$ mK the qubit is isolated from the excited states since these lie above the anticrossing point by ≈6 GHz. As illustrated in Fig. 6(b), the value of the avoided crossing depends on N_g but larger ratios $E_{J,2}/E_c$ weaken this dependence. For the parameters in Fig. 6(b) a charging energy of $\lesssim$0.1 GHz leads to nearly flat qubit levels.

At the anticrossing point defined in the DW regime the qubit eigenstates are also parity eigenstates, which satisfy $\hat{P}|\psi_0\rangle = |\psi_0\rangle$ and $\hat{P}|\psi_1\rangle = -|\psi_1\rangle$, with $\hat{P} = \exp(i\hat{N}\pi)$ being the Cooper-pair parity operator. Due to this symmetry, the qubit eigenstates have the characteristic "even-odd" probability distributions, plotted in Fig. 6(c). These distributions lead to the matrix element $\langle\psi_0|\hat{N}|\psi_1\rangle = 0$ and, because $\partial H/\partial N_g = -8E_c\hat{N}$ ($N_g = 0$), the relaxation due to

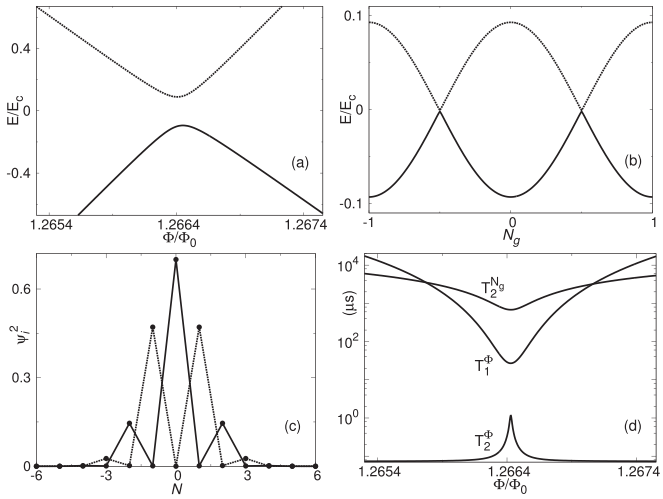

FIG. 6. (a) Energy levels of parity-protected qubit (double well) as a function of magnetic flux forming an anticrossing at $\Phi/\Phi_0 \approx 1.2664$. (b) Qubit levels as a function of N_g at anticrossing. (c) Distributions of qubit states at anticrossing. (d) Limiting timescales. In all panels $E_c = 0.35$ GHz and $N_g = 0$ unless otherwise stated. For clarity in panels (a) and (b), the energies are shifted near $E = 0$.

charge-induced noise is suppressed, $\Gamma_1^{N_g} = 0$. This property is one of the main advantages of the parity-protected qubit in the DW compared with the gatemon qubit in the SW. The even-odd distributions at the anticrossing point are exact when the DW is defined uniquely by $E_{J,2}$, namely, $V_J(\varphi_0) = E_{J,2}\cos(2\varphi_0)$, thus $[\hat{P}, H] = 0$. The qubit Hamiltonian [Eq. (14)] contains various $E_{J,M}$ terms making the even-odd distributions only approximately valid. The approximation is nevertheless particularly accurate as seen in Fig. 6(c) and remains applicable to the different junction parameters we have explored.

The results for the coherence times of the parity-protected qubit in the vicinity of the anticrossing point are presented in Fig. 6(d). These results demonstrate that dephasing due to flux-induced noise T_2^Φ is the limiting timescale. In contrast with the gatemon qubit, now both $\Gamma_1^{N_g}$ and Γ_1^p are suppressed because of the DW symmetries; the corresponding matrix elements are zero. The anticrossing point can be considered as a flux sweet spot where T_2^Φ is an order of magnitude longer compared with T_2^Φ away from the anticrossing. In addition, larger values of E_c tend to increase T_2^Φ as they produce a smoother anticrossing. The results in Fig. 6(d) are for $N_g = 0$ which defines the charge sweet spot. For $N_g \neq 0$ we have observed no improvement in the coherence times while simultaneously $\Gamma_1^{N_g} \neq 0$ and $\Gamma_1^p \neq 0$. According to our calculations in Appendix F the latter range from $T_1^p > 1$ s near $N_g = 0$ to $T_1^p \approx 10$ ms as we approach $N_g = 0.5$. For the parity-protected qubit we can also consider relaxation and dephasing due to fluctuations in the chemical potential at a fixed magnetic flux. Assuming again that $A_\mu \sim A_\Phi$ and focusing on the anticrossing, we find that the times $T_{1,2}^\mu$ are at least two orders of magnitude longer than the corresponding $T_{1,2}^\Phi$. This result indicates that magnetic flux fluctuations is the limiting noise source.

Although our estimates are for specific NW parameters and noise amplitudes, we expect the change from a T_2^μ-limited qubit in the SW regime to a T_2^Φ-limited qubit in the DW regime to be general enough. We also expect that longer coherence times in the DW regime can be obtained with some simple parameter optimization. Interestingly, a qubit formed with two NW-based junctions in a SQUID configuration [14] can reach relaxation times of $T_1 \approx 7$ μs in the parity-protected regime, in contrast with $T_1 \approx 0.6$ μs outside the protected regime. However, we emphasize that in this SQUID the flux enters very differently as compared with our qubit system.[4] In particular, in Ref. [14] the flux is tuned to $\Phi/\Phi_0 = 1/2$, which in practice requires a relatively large SQUID loop enhancing the sensitivity to flux noise. In contrast, the flux in our qubit system enters through the axial magnetic field applied to the NW. These considerations are expected to lead to different behaviors against flux fluctuations, and hence in the resulting T_1^Φ and T_2^Φ times. Having clarified the above differences, we expect the physical behavior of these two qubits to be relatively similar near the anticrossing (see also Ref. [42]).

V. DISCUSSION AND CONCLUSIONS

We considered a Josephson junction formed in a full-shell NW and demonstrated that we can change the Josephson potential from a SW to a DW potential by tuning the applied magnetic flux threading the NW section. These potential wells can serve as the basis of a gatemon qubit and a parity-protected qubit, respectively. The protected qubit studied in our work is defined in a single Josephson junction and is arguably advantageous compared with more complex geometries proposed earlier and based on interferometers.

Some of the conclusions of our study that could be relevant towards the experimental implementation of these ideas include: (i) NWs with small radii, e.g., < 60 nm, are generally better to find a DW regime and define a parity-protected qubit. In these NWs the DW is formed away from the lobe's boundary, thus the flux modulation of the pairing potential due to the LP effect has a negligible role. For NWs with large radii the formation of a DW potential depends on the strength of the LP effect and the coherence length of the superconducting shell. (ii) We have studied junctions with lengths of 100–200 nm and found that the DW is more likely to arise in long junctions. The reason is that the energy levels lying above the superconducting gap are actively involved in the formation of the DW and their role becomes more significant as the junction length increases.

Qubit experiments based on full-shell NWs [25–27] typically find short timescales $T_1 \approx 0.5$–1 μs. This might be caused by the quasiparticle poisoning enhancement near $\Phi/\Phi_0 \approx 1$ due to the increased density of subgap states [41]. It is interesting though, that the density of the subgap states is gate-tunable and that recent experiments have demonstrated their coherent control with transitions yielding relaxation times $T_1 \approx 3$–5 μs [26]. These encouraging results demon-

[4]It is useful to compare Eq. (2) in Ref. [14], where the flux enters as a phase modulation, $\varphi_0 \to \varphi_0 - 2\pi\Phi/\Phi_0$, with our Eqs. (8), (9), and (10) where the flux enters as a linear shift.

strate that the combined gate and flux tunability of full-shell NW Josephson junctions could offer a wide range of possibilities when designing qubits. Furthermore, simulations [35] beyond the hollow-core model show a rich phenomenology that includes 0, π, and ϕ_0 junctions that could be exploited for qubit designs. Also, the flux modulation of ABSs is not unique to full-shell NWs, since a magnetic field parallel to the NW causes orbital effects [34], and thus a flux-dependent qubit frequency [43].

ACKNOWLEDGMENTS

We acknowledge the support of the Spanish Ministry of Science through Grants PID2021-125343NB-I00 and TED2021-130292B-C43 and PID2022-140552NA-I00 funded by MCIN/AEI/10.13039/501100011033, "ERDF A way of making Europe," the Spanish Comunidad de Madrid "Talento Program" (Project No. 2022-T1/IND-24070), and European Union NextGenerationEU/PRTR. We acknowledge the support of the CSIC's Quantum Technologies Platform (QTEP). Support from the CSIC Interdisciplinary Thematic Platform (PTI+) on Quantum Technologies (PTI-QTEP+) is also acknowledged.

DATA AVAILABILITY

The data that support the findings of this article are not publicly available upon publication because it is not technically feasible and/or the cost of preparing, depositing, and hosting the data would be prohibitive within the terms of this research project. The data are available from the authors upon reasonable request.

APPENDIX A: DETAILED DESCRIPTION OF FULL-SHELL NANOWIRE

We consider a semiconducting NW with cylindrical symmetry and assume within the hollow-core approximation [24] that the electrons are confined near the surface of the NW. Working in cylindrical coordinates (r, φ, z) with the unit vectors $(\hat{e}_r, \hat{e}_\varphi, \hat{e}_z)$ the hollow-core approximation allows us to fix the radial coordinate, $r = R_0$, where R_0 is the radius of the NW. As a result, the flux threading the cross section of the NW is $\Phi = \pi B R_0^2$ with B being the magnitude of the applied magnetic field along the direction of the NW; $\vec{B} = B\hat{e}_z$. The magnetic vector potential in the azimuthal direction is

$$\vec{A} = A_\varphi \hat{e}_\varphi = \frac{\Phi}{2\pi R_0}\hat{e}_\varphi, \tag{A1}$$

and the Hamiltonian of the NW is

$$H_0 = \frac{(\vec{p} + e\vec{A})^2}{2m^*} - \mu + H_{\rm SO}, \tag{A2}$$

where m^* is the effective mass, μ is the chemical potential, and the momentum operator has the form

$$\vec{p} = \left(p_\varphi, p_z\right) = \left(-\frac{i\hbar}{R_0}\partial_\varphi, -i\hbar\partial_z\right). \tag{A3}$$

The Rashba spin-orbit (SO) Hamiltonian is

$$H_{\rm SO} = \frac{\alpha_{\rm so}}{\hbar}[p_z\sigma_\varphi - (p_\varphi + eA_\varphi)\sigma_z] \tag{A4}$$

and comes from radial inversion symmetry breaking, i.e., $\vec{\alpha} = \alpha_{\rm so}\hat{e}_r$. Finally $\sigma_\varphi = (\sigma_y \cos\varphi - \sigma_x \sin\varphi)$ and σ_z are spin-1/2 Pauli matrices.

The semiconducting NW is wrapped by a thin superconducting shell and, due to the proximity effect, it acquires superconducting pairing terms. An applied magnetic flux modulates the induced superconductivity via the Little-Parks effect which in turn induces a winding of the superconducting phase in the shell around the NW axis, $\Delta(\vec{r}) = \Delta(r)e^{in\varphi}$. The amplitude Δ, with $r = R_0$, and the winding number n depend on the applied magnetic flux (Appendix B). Denoting by $\Phi_0 = h/2e$ the flux quantum, the winding number is equal to the nearest integer to Φ/Φ_0, i.e., $n = 0, \pm1, \pm2, \ldots$. We can then use the variable $\phi = n - \Phi/\Phi_0$ to measure deviations from integer fluxes and also label with n the so-called LP lobes [32].

The Bogoliubov-de-Gennes Hamiltonian describing the proximitized NW can be written as decoupled Hamiltonians characterized by the eigenvalues m_j of a generalized angular-momentum operator [24] $J_z = -i\partial_\varphi + \frac{1}{2}\sigma_z + \frac{1}{2}n\tilde{\tau}_z$ (with $\hbar = 1$ and $\tilde{\tau}_z$ acts in Nambu space). For odd n, $m_j = 0, \pm1, \ldots$, and for even n, $m_j = \pm1/2, \pm3/2, \ldots$. The final BdG Hamiltonian for a given m_j can be written in the compact matrix form

$$H_{\rm BdG} = \begin{pmatrix} H^+ & H^z_{\rm SO} \\ -H^z_{\rm SO} & H^- \end{pmatrix}, \tag{A5}$$

with the 2×2 matrices

$$H^z_{\rm SO} = \begin{pmatrix} -\alpha_{\rm so}\partial_z & 0 \\ 0 & \alpha_{\rm so}\partial_z \end{pmatrix}, \tag{A6}$$

and

$$H^+ = \begin{pmatrix} \frac{p_z^2}{2m^*} + \mu_e^+ & \Delta \\ \Delta^* & -\frac{p_z^2}{2m^*} + \mu_h^+ \end{pmatrix}. \tag{A7}$$

The Hamiltonian H^- has the same form as H^+ but with $\mu_e^+ \to \mu_e^-$ and $\mu_h^+ \to \mu_h^-$. The flux-dependent effective potentials are

$$\mu^+_{e(h)}(\phi) = \mu^{0+}_{e(h)} + \delta^+(\phi) \pm \frac{\hbar^2}{8m^*R_0^2}\phi^2,$$
$$\mu^-_{e(h)}(\phi) = \mu^{0-}_{e(h)} + \delta^-(\phi) \pm \frac{\hbar^2}{8m^*R_0^2}\phi^2, \tag{A8}$$

and at the center of a lobe ($\phi = 0$) we have

$$\mu_e^{0\pm} = -\mu + \frac{(1 \mp 2m_j)^2\hbar^2}{8m^*R_0^2} + \frac{(1 \mp 2m_j)\alpha_{\rm so}}{2R_0}, \tag{A9}$$

with $\mu_h^{0+} = -\mu_e^{0+}$ and $\mu_h^{0-} = -\mu_e^{0-}$. Finally, the linear terms are

$$\delta^\pm(\phi) = \frac{(-2m_j \pm 1)\hbar^2}{4m^*R_0^2}\phi \pm \frac{\alpha_{\rm so}}{2R_0}\phi, \tag{A10}$$

which dominate for small fluxes near the center of a lobe. For each m_j, the BdG Hamiltonian produces two subgap modes originating from the Hamiltonians H^+ and H^-. At low chemical potentials only one mode lies in the superconducting gap, while an increase of the order of $\mu_e^{0-} - \mu_e^{0+}$ puts the second

mode into the gap [33]. For $\alpha_{so} = 0$ degenerate BdG energy levels occur because $\mu_e^{0+}(m_j + 1) = \mu_e^{0-}(m_j)$ [33].

To obtain the eigenvalues of H_{BdG}, we expand the BdG solution in electron-hole basis states $|u_i\rangle$ ($\Delta = 0$), calculate the matrix elements $\langle u_j|H_{\mathrm{BdG}}|u_i\rangle$, and finally diagonalize the resulting BdG matrix. The average energy spacing of the basis states with respect to Δ determine the required number of basis states (a few hundreds). This number decreases in the presence of the Little-Parks effect making the method more powerful. The exact BdG model is needed in order to account for the energy levels which lie outside the superconducting gap. We emphasize that without these levels the Josephson potential cannot be accurately computed.

APPENDIX B: FLUX MODULATION OF PAIRING POTENTIAL

In full-shell NWs the LP effect results in a flux dependent pairing potential term, $\Delta = \Delta(\Phi)$. The flux dependence can be derived from the expression [44]

$$\ln\frac{\Delta}{\Delta_0} = -\frac{\pi}{4}\frac{\Lambda}{\Delta}, \quad \Lambda \leqslant \Delta,$$
$$\ln\frac{\Delta}{\Delta_0} = -\ln\left(\frac{\Lambda}{\Delta} + \sqrt{(\Lambda/\Delta)^2 - 1}\right) + \frac{\sqrt{(\Lambda/\Delta)^2 - 1}}{2(\Lambda/\Delta)} - \frac{\Lambda}{2\Delta}\arctan\frac{1}{\sqrt{(\Lambda/\Delta)^2 - 1}}, \quad \Lambda \geqslant \Delta. \tag{B1}$$

Δ_0 denotes the value of Δ at zero flux and Λ is the flux-dependent pair-breaking term $\Lambda = \Lambda(\Phi)$. Assuming that the thickness of the superconducting shell is much smaller than the radius R_0 then, to a good approximation,

$$\Lambda(\Phi) \approx \frac{4\xi^2 k_B T_c}{\pi R_0^2}\left(n - \frac{\Phi}{\Phi_0}\right)^2, \tag{B2}$$

where n is the lobe index, T_c is the zero-flux critical temperature, ξ is the coherence length of the superconducting shell and $k_B T_c = \Delta_0/1.76$. Equation (B1) is solved numerically and some typical examples of the pairing potential as a function of the magnetic flux are shown in Fig. 7. Larger values of ξ lead the junction to the destructive regime where $\Delta = 0$ for $\Lambda \gtrsim \Delta_0/2$.

APPENDIX C: ADDITIONAL EXAMPLES OF JOSEPHSON POTENTIALS

In this Appendix we present additional examples of the Josephson potential. We consider a NW with $R_0 = 50$ nm and study the most general case where $\Delta = \Delta(\Phi)$. We gradually tune the junction to the destructive regime by increasing ξ and compute the Josephson potential from the BdG Hamiltonian. We focus on the DW regime and show the results in Figs. 8(a) and 8(b). It can be seen that the LP effect induces a small decrease in the potential barriers but the overall shape of the DW remains unaffected even for relatively large values of ξ (120 nm) that lead the junction to the destructive regime. Our analysis indicates that this is a general result, namely, for a NW with a small radius the LP effect has no significant role.

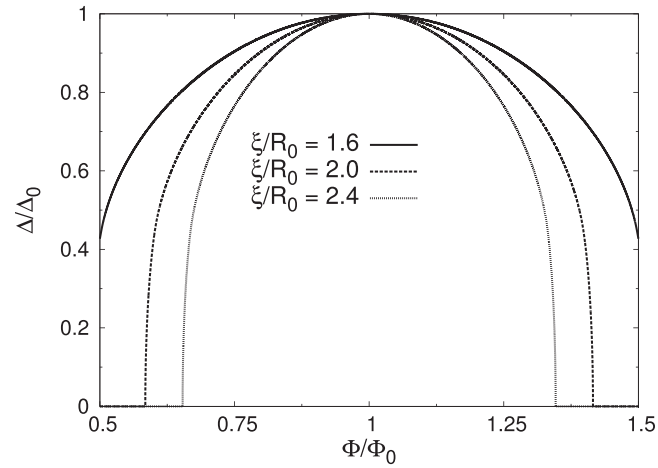

FIG. 7. Pairing potential as a function of magnetic flux for different ratios ξ/R_0, where ξ is the coherence length of the superconducting shell and R_0 is the radius of the semiconducting NW.

The DW Josephson potentials studied in Sec. III are for zero temperature, however, a DW Josephson potential can also be formed at finite temperatures. To demonstrate this argument we focus on realistic temperatures for superconducting qubits, $T \lesssim 30$ mK, and present in Fig. 8(c) an example of a DW potential at $T = 15$ mK. Compared with $T = 0$ K (see Fig. 3) the finite temperature has a negligible effect. This result is in agreement with an earlier study of the critical current at $T \neq 0$ K in full-shell NWs [33]. Finally, we take into account the Zeeman effect due to the applied magnetic field B. Here, we include the Zeeman term $g\mu_B B\sigma_z/2$ in the BdG Hamiltonian, Eq. (A5), where g is the Landé g factor of the NW and μ_B is the Bohr magneton. We have explored different junctions giving rise to DW Josephson potentials in the first LP lobe; one example is presented in Fig. 8(d). Based on our numerical investigation we conclude that including a small Zeeman term in the BdG Hamiltonian tends to produce

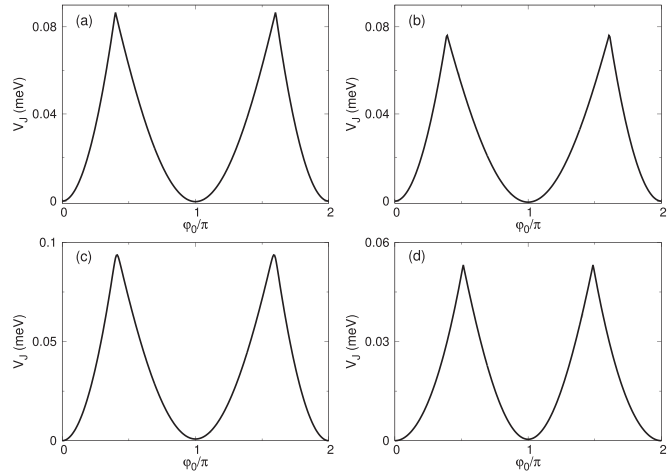

FIG. 8. Examples of double-well Josephson potentials. (a) $\Delta = \Delta(\Phi)$ with $\xi = 80$ nm, (b) $\Delta = \Delta(\Phi)$ with $\xi = 120$ nm, (c) $\Delta = \Delta_0 = 0.2$ meV at finite temperature $T = 15$ mK, and (d) $\Delta = \Delta_0 = 0.2$ meV including a Zeeman term with g factor $g = 10$. Parameters: $L_S = 2000$ nm, $L_N = 100$ nm, and $R_0 = 50$ nm.

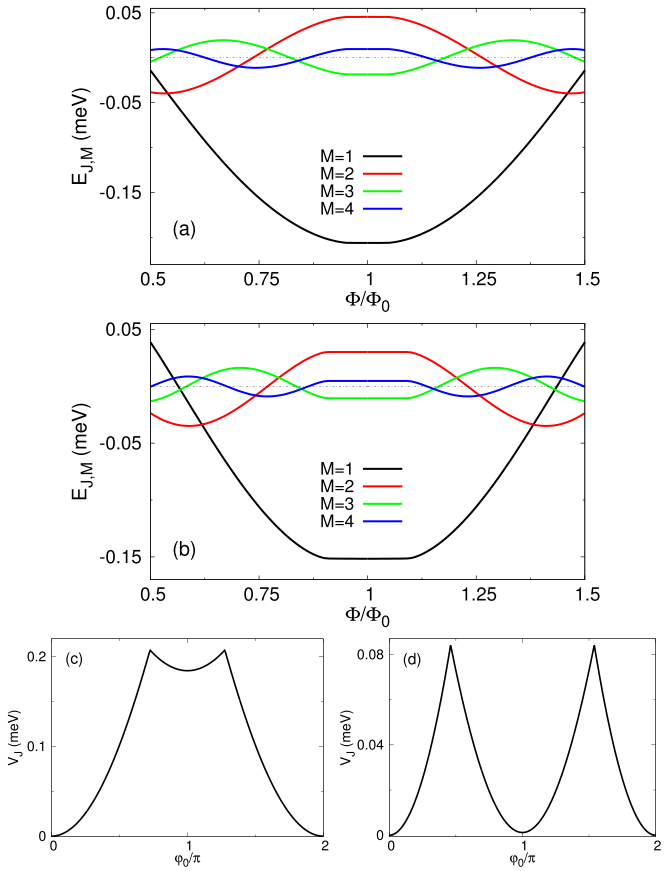

FIG. 9. (a) Fourier components of Josephson potential for $M = 1$–4 as a function of magnetic flux for $\Delta = \Delta(\Phi)$, $\xi = 50$ nm, and $L_N = 100$ nm. (b) As in panel (a) but for $L_N = 200$ nm. Josephson potential for $\Delta = \Delta(\Phi)$, $\xi = 50$ nm, and $L_N = 200$ nm at different fluxes: (c) $\Phi/\Phi_0 = 1.25$, and (d) 1.44. Parameters: $L_S = 2000$ nm, and $R_0 = 75$ nm.

weaker Josephson potentials due to the rearrangement of the flux dependent potentials $\mu_e^{\pm}$ and $\mu_h^{\pm}$. However, following the general arguments given in Sec. III we can always form a flux tunable DW potential for realistic g-factor values, $g \lesssim 20$. Furthermore, with a fine tuning of the parameters, such as R_0, ξ, g, and L_N, the Zeeman term can lead to more symmetric DW potentials, although this special case cannot be always guaranteed.

According to the description in Sec. III a longer Josephson junction can be advantageous to form a DW potential. In Fig. 9 we show one typical example comparing two junctions with different L_N lengths. Tuning the magnetic flux forms a DW with nearly equal potential minima [Fig. 9(d)] only for the longer junction ($L_N = 200$ nm). This example confirms the significance of the energy levels lying above the superconducting gap.

Deviations from the cylindrical symmetry of the NW, for example due to disorder, can affect the flux dependence of the BdG levels and the resulting Josephson potential. To account for this aspect we introduce a coupling between the BdG energy levels that come from different angular numbers m_j. Specifically, in the BdG Hamiltonian [Eq. (A5)] we couple the electron states with the same spin component but with different m_j. We consider this coupling between nearest m_j numbers and follow the same procedure for the hole states. We explore the simplest regime where the coupling strength, q, is assumed to be constant along the entire length of the junction. Although this regime is probably not the most realistic, it gives valuable insight into how robust the Josephson potential is to weak asymmetries due to possible disorder and/or geometrical imperfections in the NW.

For a NW with $R_0 = 50$ nm, $\Delta = \Delta_0 = 0.2$ meV, and $q = 0$ a DW potential is formed at $\Phi/\Phi_0 \approx 1.26$ (Sec. III). Increasing q gradually shifts the DW to lower fluxes until the DW eventually reaches the lobe's center. A further increase in q destroys the DW potential. This means that an anticrossing point between the qubit levels as in Fig. 6(a) can no longer be defined. For example, $q = 0.12$ meV results in a DW at $\Phi/\Phi_0 \approx 1.12$ but $q = 0.15$ meV gives no DW. According to Sec. III, for a NW with $R_0 = 75$ nm, $\Delta = \Delta_0 = 0.2$ meV, and $q = 0$ there is no DW. Our calculations show that $q = 0.055$ meV gives rise to a DW at the lobe's boundary, $\Phi/\Phi_0 \approx 1.5$. Increasing the coupling strength to $q = 0.12$ meV shifts the DW to a lower flux, i.e., $\Phi/\Phi_0 \approx 1.19$ and eventually $q = 0.15$ meV destroys the DW potential. This numerical investigations demonstrates that the Josephson potentials studied in Sec. III remain robust when a small coupling, $q \lesssim \Delta_0/2$, is introduced (for any physical reason) between the BdG energy levels of the original symmetric NW. We remark that much stronger couplings can be assumed as long as q is taken to be nonzero only within a small region of the junction.

APPENDIX D: EFFECT OF SPIN-ORBIT COUPLING ON JOSEPHSON POTENTIAL

A nonzero spin-orbit coupling in the radial direction, $\alpha_{so} \neq 0$, breaks the degeneracy of the $m_j = 0$ and $m_j = \pm 1$ energy levels. In this Appendix we demonstrate that a symmetric DW potential can still be formed independent of this degeneracy. We consider a relatively small coupling, $\alpha_{so} = 20$ meV nm, and assume this coupling to be uniform along the junction. Gate-induced electric fields in the N region may introduce some degree of nonuniformity but this is not expected to drastically modify the Josephson potential provided the length of the N region is small.

In Fig. 10 we present a case where a DW Josephson potential is formed. We see that the overall flux dependence of the Fourier components $E_{J,M}$ is similar to the case with $\alpha_{so} = 0$ [Figs. 3(a) and 4(a)] studied in the main text. Furthermore, the DW potential leads to an anticrossing between the two lowest qubit levels at $\Phi/\Phi_0 \approx 1.375$. We have confirmed that similar trends can be found for different chemical potentials and spin-orbit couplings.

Although it is not the main topic of our study a noteworthy difference from the $\alpha_{so} = 0$ case can be observed when the NW is in the topological regime and the $m_j = 0$ mode gives rise to a pair of Majorana states. The properties of these states and their exact flux dependence in full-shell NWs have been studied in detail in previous theoretical works [24,45–47]. Following the arguments in these works it can be shown that the appearance of Majorana states can result in a triple-well Josephson potential, as demonstrated in Fig. 10. The

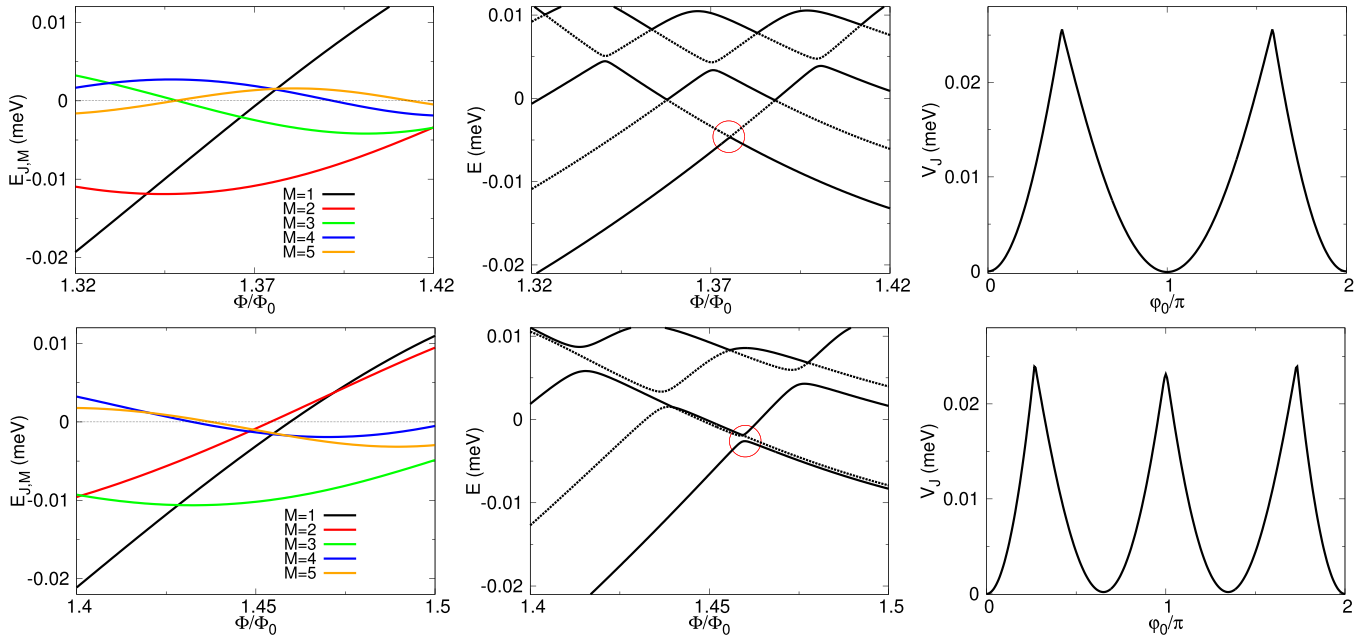

FIG. 10. Fourier components of Josephson potential, energy levels of qubit Hamiltonian [Eq. (14)], and Josephson potential at the flux defining the lowest anticrossing. (upper panels) Double-well regime at $\mu = 0.2$ meV. (lower panels) Triple-well regime at $\mu = 0.5$ meV. Parameters: $L_S = 2000$ nm, $L_N = 100$ nm, $R_0 = 50$ nm, $\alpha_{so} = 20$ meV nm, and $\Delta = \Delta_0 = 0.2$ meV.

potential barrier centered at $\varphi_0 = \pi$ is indicative of the Majorana states. In the triple-well regime the component $E_{J,3}$ is the dominant one and provided $E_c \ll E_{J,3}$ the system Hamiltonian [Eq. (14)] has three quasidegenerate ground levels. In Fig. 10 the charging energy is $E_c = 0.1$ GHz and similar to the DW a smaller E_c tends to close the observed energy gap at $\Phi/\Phi_0 \approx 1.46$. According to our calculations the strength and symmetry of the triple well depend sensitively on the exact junction parameters as well as the LP effect. In addition, for an accurate treatment of the Majorana states a three-dimensional model seems to be necessary [46–48]. For these reasons we do not consider the hollow-core model to be adequate to capture details of the triple-well potential and therefore do not further explore this regime in our work.

APPENDIX E: JOSEPHSON POTENTIAL DERIVED FROM SIMPLIFIED MODEL

In this Appendix we explore in some detail the DW Josephson potential derived from the simplified junction model introduced in Sec. III. For clarity of presentation we focus on the realistic limits $\tau_a \lesssim 0.5$ and $\tau_s \gtrsim 0.75$, which are in agreement with our BdG calculations. Focusing on the range $(0, \pi)$ a simple investigation of the Josephson potential shows that the angle θ:

$$\theta = 2\sin^{-1}\sqrt{\frac{1}{\tau_s}\left(1 - \frac{\gamma^2(\Phi_{\rm DW})}{\Delta^2(\Phi_{\rm DW})}\right)}, \tag{E1}$$

at which

$$E_{-,s}(\theta, \Phi_{\rm DW}) = 0, \tag{E2}$$

defines the position of the left potential barrier. The corresponding barrier height is equal to

$$V_{\rm B} = E_{+,a}(\theta, \Phi_{\rm DW}) - E_{+,a}(\pi, \Phi_{\rm DW}), \tag{E3}$$

and this increases for smaller values of θ. Substituting Eq. (12) into Eq. (E1) we derive that

$$\theta = 2\sin^{-1}\sqrt{\frac{\tau_a}{\tau_s}}, \tag{E4}$$

and Eq. (E3) gives the barrier height

$$V_{\rm B} = \left(\sqrt{1 - \tau_a^2/\tau_s} - \sqrt{1 - \tau_a}\right)\Delta(\Phi_{\rm DW}). \tag{E5}$$

Thus the limit $\tau_s \to 1$ leads to the maximum height, and for the special case $\tau_s = 2\tau_a$ the left potential barrier is centered at $\theta = \pi/2$ leading to the most symmetric DW profile.

The flux dependence of the Fourier components can be written as follows:

$$E_{J,M}(\Phi) = X_M(\Phi) + E_{J,M}(\Phi_0)\frac{\Delta(\Phi)}{\Delta_0}, \tag{E6}$$

with

$$X_M(\Phi) = -\frac{1}{\pi}\int_{\pi-\delta}^{\pi+\delta} E_{-,s}(\varphi_0, \Phi)\cos(M\varphi_0)d\varphi_0, \tag{E7}$$

and $\delta = \delta(\Phi)$. If $E_{-,s} < 0$ (>0) for any φ_0 then $\delta = 0$ (π); otherwise, the value of δ is found from the condition $E_{-,s}(\pi - \delta, \Phi) = 0$ with $\pi - \delta = \theta$ at $\Phi = \Phi_{\rm DW}$. The term $X(\Phi)$ quantifies the effect of $\gamma(\Phi)$ on the Josephson potential, thus, assuming $\gamma(\Phi) = 0$ we have $\delta = 0$. As a result, the flux dependence of $E_{J,M}(\Phi)$ is determined solely by the second term in Eq. (E6) which is due to the LP effect.

In the limit $\tau_s \to 1$ the modulation of the Josephson potential due to $\gamma(\Phi)$ can be analytically computed, and the final

result is

$$X_M(\Phi) = -\Delta(\Phi)\mathcal{I}_M + \gamma(\Phi)\mathcal{J}_M, \tag{E8}$$

with the flux-dependent terms

$$\mathcal{I}_M = C_M\left(1 - \cos\frac{\delta}{2}\cos M\delta\right) + D_M \sin\frac{\delta}{2}\sin M\delta, \tag{E9}$$

$$\mathcal{J}_M = 2(-1)^{M+1}\frac{\sin M\delta}{\pi M}, \tag{E10}$$

and the constants

$$C_M = \frac{(-1)^M}{\pi(1/4 - M^2)}, \quad D_M = \frac{2M(-1)^{M+1}}{\pi(1/4 - M^2)}. \tag{E11}$$

When $\gamma(\Phi) \approx 0$ we derive that $\mathcal{I}_M = \mathcal{J}_M \approx 0$ thus the LP effect dominates.

We now present some results obtained from the simplified model. Assuming the parameters $\tau_s = 0.99$, $\tau_a = 0.40$, and $\beta = 0.46$ then for $\Delta(\Phi) = \Delta_0$ Eq. (12) is satisfied when $R_0 = 50$ nm. Thus, by tuning the flux a DW potential is formed at $\Phi/\Phi_0 \approx 1.31$. In contrast, when $R_0 = 75$ nm a DW cannot be formed because Eq. (12) is not satisfied at any flux value within the first lobe. However, when the LP effect is taken into account with $\xi = 110$ nm, then Eq. (12) is satisfied and a DW with equal potential minima can be formed at $\Phi/\Phi_0 \approx 1.44$. This flux value is sensitive to ξ and typically decreases with ξ. This result qualitatively agrees with the BdG model and demonstrates that the LP effect can favor the formation of a DW potential.

A general observation, independent of the LP effect, is that the SW potential at $\Phi/\Phi_0 = 1$ is determined mainly by $E_{-,s}$, whereas the SW potential at $\Phi/\Phi_0 \approx 1.5$ is the result of $E_{+,a}$. For this reason the potential at $\Phi/\Phi_0 \approx 1.5$ is always swallower and shifted by π compared with that at $\Phi/\Phi_0 = 1$. This observation is in agreement with the exact Josephson potential in Fig. 3, derived from the BdG Hamiltonian.

In Fig. 11(a) we plot the first few Fourier components of the Josephson potential as a function of the magnetic flux for one typical junction. The overall flux dependence has the same characteristics as those obtained from the BdG model. When considering the LP effect on the superconducting pairing a symmetric DW potential is formed. As described in Sec. III, NWs with large radii can induce only asymmetric DWs unless the coherence length ξ of the shell has a suitable value. In Fig. 11(b), we quantify this value for different radii by numerically solving Eq. (12). For $R_0 < 64$ nm the value of ξ is not relevant, namely, a constant pairing potential suffices to form a symmetric DW. The NW with $R_0 = 50$ nm studied in Sec. III is one example of this category. In contrast, for $R_0 \gtrsim 64$ nm the value of ξ is relevant and rather large values are necessary to form a DW as illustrated in Fig. 11(b). The NW with $R_0 = 75$ nm (Sec. III) belongs to this category. In Fig. 11(b), we plot the value of ξ required to form the DW potential at the lobe's boundary, $\Phi/\Phi_0 = 1.5$. A larger ξ is needed to shift the DW potential closer to the center. Because the value of ξ is not controllable, we conclude that NWs with small radii should be advantageous to probe a parity-protected qubit.

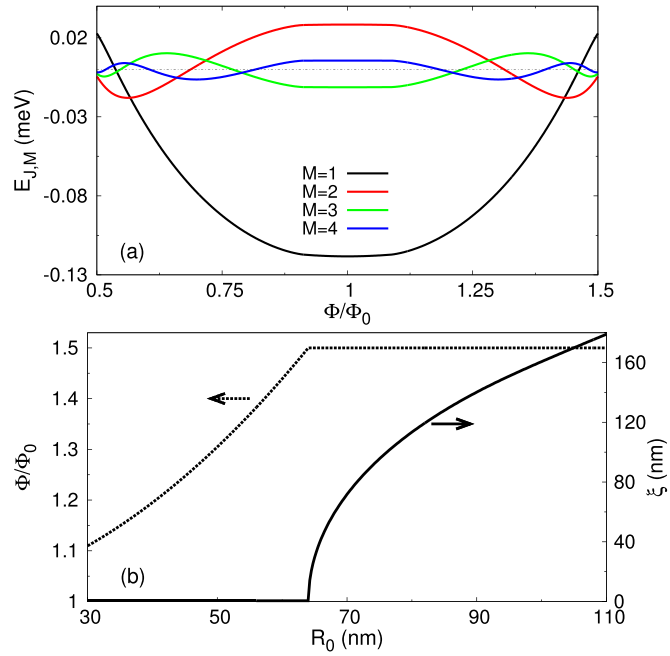

FIG. 11. (a) Fourier components of Josephson potential derived from simplified model with $R_0 = 75$ nm, $\Delta = \Delta(\Phi)$, and $\xi = 110$ nm. (b) (left axis) Flux resulting in DW for $\Delta = \Delta_0 = 0.2$ meV when $R_0 < 64$ nm. When $R_0 \gtrsim 64$ nm, $\Delta = \Delta(\Phi)$ is needed to define a DW. (right axis) The required ξ to form a DW at $\Phi/\Phi_0 = 1.5$ (a smaller Φ requires a larger ξ).

APPENDIX F: FURTHER ANALYSIS OF PARITY-PROTECTED QUBIT

In the DW regime the ratio $E_{J,2}/E_c$ determines the parity-protected qubit energy levels. These levels become quasidegenerate as the charging energy decreases leading to the closing of the anticrossing gap (Fig. 12). This result can be understood by writing the qubit Hamiltonian, Eq. (14), in φ_0 space and noticing that the "kinetic term" is proportional to E_c. Additional insight can be gained by using an approximate model where the qubit states are written as a superposition of two basis states. For this purpose we choose the (lowest) SW states at $\Phi/\Phi_0 = 1$ and $\Phi/\Phi_0 = 1.5$, where $E_{J,1}$ is the dominant term [Figs. 3(b) and 3(e)]. We denote the basis states at these two flux values by $|y_1\rangle$ and $|y_2\rangle$, respectively. Despite the simplicity of the model the approximate energies in Fig. 12 agree very well with the exact energies [calculated from Eq. (14)] and correctly predict the closing of the anticrossing gap. In the Cooper pair basis $|N\rangle$ we write the states

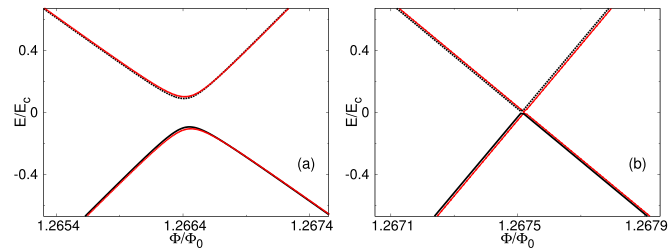

FIG. 12. Exact (black) and approximate (red) energy levels of parity-protected qubit as a function of magnetic flux for charging energy: (a) $E_c = 0.35$ GHz, and (b) 0.12 GHz.

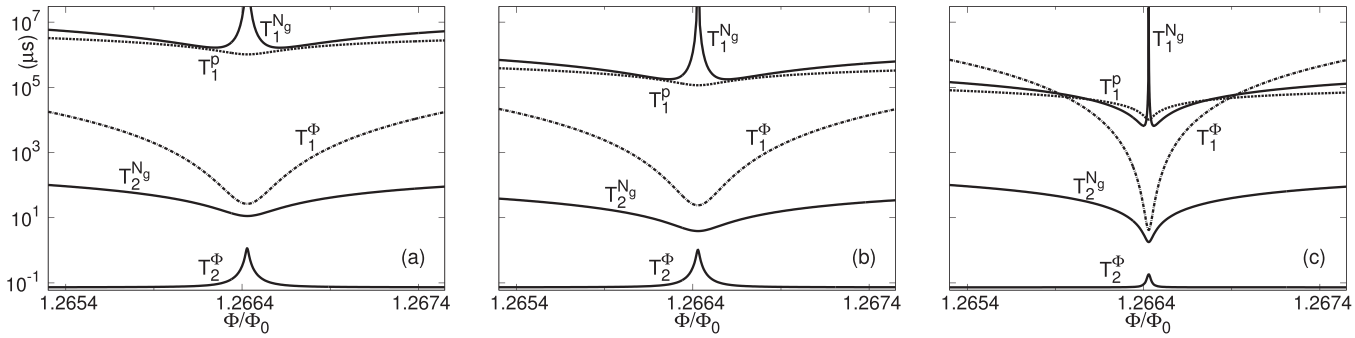

FIG. 13. As in Fig. 6(d) main text but for nonzero offset charge: (a) $N_g = 0.05$, (b) 0.15, and (c) 0.45.

as $|y_k\rangle = \sum_N C_N^k |N\rangle$, $k = 1, 2$ so the gap derived from the approximate model is

$$E_1 - E_0 = \frac{2}{1-s^2}[(x_{1,2} - sx_{2,2})(x_{1,2} - sx_{1,1})]^{1/2}, \quad \text{(F1)}$$

where E_0 and E_1 are the qubit levels at the anticrossing. Here, $s = \langle y_1|y_2\rangle$, and the matrix elements (for $N_g = 0$) are

$$x_{i,j} = \sum_{N,M} \frac{1}{2} E_{J,M}\left(C_N^i C_{N+M}^j + C_N^j C_{N+M}^i\right) + 4E_c \sum_N N^2 C_N^i C_N^j. \quad \text{(F2)}$$

Knowledge of C_N^m allows us to determine the gap for any flux dependence of $E_{J,M}$. For the approximate results in Fig. 12 C_N^m are found numerically but approximate methods can also be applied. The anticrossing gap given by Eq. (F1) is computed at the flux satisfying the equality $x_{1,1} = x_{2,2}$, which gives the position of the anticrossing point. This analysis indicates that since the effective widths of the two potential wells forming the DW Josephson potential (Sec. III) are generally unequal, the two potential minima centered at $\varphi_0 = 0$ and π have to be slightly detuned at the anticrossing.

Finally, we investigate the qubit Hamiltonian [Eq. (14)] for $N_g \neq 0$ and show the coherence times of the parity protected qubit in Fig. 13. Compared with $N_g = 0$, [Fig. 6(d) main text] now away from the anticrossing point we have $\langle\psi_0|\partial H/\partial N_g|\psi_1\rangle \neq 0$ leading to a finite relaxation time $T_1^{N_g}$. The same reasoning applies for T_1^p at any magnetic flux. The parity protection, $\Gamma_1^{N_g} \approx 0$, is again valid at the anticrossing regardless of N_g. The characteristic peak in $T_1^{N_g}$ which is observed for all N_g values in Fig. 13 is the result of this protection. When $N_g \neq 0$ dephasing due to charge-induced noise becomes stronger but again the shortest timescale of the qubit is T_2^Φ (flux-induced dephasing). At the anticrossing point and $N_g = 0.45$ the time T_2^Φ decreases by nearly an order of magnitude compared with $N_g = 0$. This decrease is related to the fact that the anticrossing becomes sharper with N_g so $D_{\Phi\Phi}$ in Eq. (19) increases. The basic conclusion is that $N_g = 0$ is the optimum offset charge value for the parity-protected qubit.

[1] M. Mohseni, A. Scherer, K. G. Johnson, O. Wertheim, M. Otten, N. A. Aadit, Y. Alexeev, K. M. Bresniker, K. Y. Camsari, B. Chapman, S. Chatterjee, G. A. Dagnew, A. Esposito, F. Fahim, M. Fiorentino, A. Gajjar, A. Khalid, X. Kong, B. Kulchytskyy, E. Kyoseva, R. Li, P. A. Lott, I. L. Markov, R. F. McDermott, G. Pedretti, P. Rao, E. Rieffel, A. Silva, J. Sorebo, P. Spentzouris, Z. Steiner, B. Torosov, D. Venturelli, R. J. Visser, Z. Webb, X. Zhan, Y. Cohen, P. Ronagh, A. Ho, R. G. Beausoleil, and J. M. Martinis, How to build a quantum supercomputer: Scaling from hundreds to millions of qubits, arXiv:2411.10406.

[2] G. Q. AI and Collaborators, Quantum error correction below the surface code threshold, Nature (London) **638**, 920 (2024).

[3] J. Danon, A. Chatterjee, A. Gyenis, and F. Kuemmeth, Protected solid-state qubits, Appl. Phys. Lett. **119**, 260502 (2021).

[4] S. Das Sarma, M. Freedman, and C. Nayak, Majorana zero modes and topological quantum computation, npj Quantum Inf. **1**, 15001 (2015).

[5] R. Aguado and L. P. Kouwenhoven, Majorana qubits for topological quantum computing, Phys. Today **73**(6), 44 (2020).

[6] B. Douçot and L. B. Ioffe, Physical implementation of protected qubits, Rep. Prog. Phys. **75**, 072001 (2012).

[7] A. Gyenis, A. Di Paolo, J. Koch, A. Blais, A. A. Houck, and D. I. Schuster, Moving beyond the transmon: Noise-protected superconducting quantum circuits, PRX Quantum **2**, 030101 (2021).

[8] A. Gyenis, P. S. Mundada, A. Di Paolo, T. M. Hazard, X. You, D. I. Schuster, J. Koch, A. Blais, and A. A. Houck, Experimental realization of a protected superconducting circuit derived from the 0–π qubit, PRX Quantum **2**, 010339 (2021).

[9] P. Brooks, A. Kitaev, and J. Preskill, Protected gates for superconducting qubits, Phys. Rev. A **87**, 052306 (2013).

[10] W. C. Smith, A. Kou, X. Xiao, U. Vool, and M. H. Devoret, Superconducting circuit protected by two-cooper-pair tunneling, npj Quantum Inf. **6**, 8 (2020).

[11] A. Maiani, M. Kjaergaard, and C. Schrade, Entangling transmons with low-frequency protected superconducting qubits, PRX Quantum **3**, 030329 (2022).

[12] C. Schrade, C. M. Marcus, and A. Gyenis, Protected hybrid superconducting qubit in an array of gate-tunable Josephson interferometers, PRX Quantum **3**, 030303 (2022).

[13] W. C. Smith, M. Villiers, A. Marquet, J. Palomo, M. R. Delbecq, T. Kontos, P. Campagne-Ibarcq, B. Douçot, and Z. Leghtas,

Magnifying quantum phase fluctuations with Cooper-pair pairing, Phys. Rev. X **12**, 021002 (2022).

[14] T. W. Larsen, M. E. Gershenson, L. Casparis, A. Kringhøj, N. J. Pearson, R. P. G. McNeil, F. Kuemmeth, P. Krogstrup, K. D. Petersson, and C. M. Marcus, Parity-protected superconductor-semiconductor qubit, Phys. Rev. Lett. **125**, 056801 (2020).

[15] G.-L. Guo, H.-B. Leng, Y. Hu, and X. Liu, $0-\pi$ qubit with one Josephson junction, Phys. Rev. B **105**, L180502 (2022).

[16] C. Ciaccia, R. Haller, A. C. C. Drachmann, T. Lindemann, M. J. Manfra, C. Schrade, and C. Schönenberger, Charge-4e supercurrent in a two-dimensional InSs-Al superconductor-semiconductor heterostructure, Commun. Phys. **7**, 41 (2024).

[17] M. Valentini, R. S. Souto, M. Borovkov, P. Krogstrup, Y. Meir, M. Leijnse, J. Danon, and G. Katsaros, Subgap-state-mediated transport in superconductor–semiconductor hybrid islands: Weak and strong coupling regimes, Phys. Rev. Res. **7**, 023022 (2025).

[18] L. Banszerus, W. Marshall, C. W. Andersson, T. Lindemann, M. J. Manfra, C. M. Marcus, and S. Vaitiekėnas, Voltage-controlled synthesis of higher harmonics in hybrid Josephson junction circuits, Phys. Rev. Lett. **133**, 186303 (2024).

[19] A. Leblanc, C. Tangchingchai, Z. S. Momtaz, E. Kiyooka, J.-M. Hartmann, G. T. Fernandez-Bada, Z. Scherübl, B. Brun, V. Schmitt, S. Zihlmann, R. Maurand, E. Dumur, S. De Franceschi, and F. Lefloch, From nonreciprocal to charge-4e supercurrent in Ge-based Josephson devices with tunable harmonic content, Phys. Rev. Res. **6**, 033281 (2024).

[20] R. S. Souto, M. Leijnse, and C. Schrade, Josephson diode effect in supercurrent interferometers, Phys. Rev. Lett. **129**, 267702 (2022).

[21] P. Zhang, A. Zarassi, L. Jarjat, V. V. de Sande, M. Pendharkar, J. S. Lee, C. P. Dempsey, A. P. McFadden, S. D. Harrington, J. T. Dong, H. Wu, A. H. Chen, M. Hocevar, C. J. Palmstrøm, and S. M. Frolov, Large second-order Josephson effect in planar superconductor-semiconductor junctions, SciPost Phys. **16**, 030 (2024).

[22] A. Leblanc, C. Tangchingchai, Z. Sadre Momtaz, E. Kiyooka, J.-M. Hartmann, F. Gustavo, J.-L. Thomassin, B. Brun, V. Schmitt, S. Zihlmann, R. Maurand, É. Dumur, S. De Franceschi, and F. Lefloch, Gate- and flux-tunable $\sin(2\phi)$ Josephson element with planar-Ge junctions, Nat. Commun. **16**, 1010 (2025).

[23] L. Banszerus, C. W. Andersson, W. Marshall, T. Lindemann, M. J. Manfra, C. M. Marcus, and S. Vaitiekėnas, Hybrid Josephson rhombus: A superconducting element with tailored current-phase relation, Phys. Rev. X **15**, 011021 (2025).

[24] S. Vaitiekėnas, G. W. Winkler, B. van Heck, T. Karzig, M.-T. Deng, K. Flensberg, L. I. Glazman, C. Nayak, P. Krogstrup, R. M. Lutchyn, and C. M. Marcus, Flux-induced topological superconductivity in full-shell nanowires, Science **367**, eaav3392 (2020).

[25] D. Sabonis, O. Erlandsson, A. Kringhøj, B. van Heck, T. W. Larsen, I. Petkovic, P. Krogstrup, K. D. Petersson, and C. M. Marcus, Destructive little-parks effect in a full-shell nanowire-based transmon, Phys. Rev. Lett. **125**, 156804 (2020).

[26] A. Kringhøj, G. W. Winkler, T. W. Larsen, D. Sabonis, O. Erlandsson, P. Krogstrup, B. van Heck, K. D. Petersson, and C. M. Marcus, Andreev modes from phase winding in a full-shell nanowire-based transmon, Phys. Rev. Lett. **126**, 047701 (2021).

[27] O. Erlandsson, D. Sabonis, A. Kringhøj, T. W. Larsen, P. Krogstrup, K. D. Petersson, and C. M. Marcus, Parity switching in a full-shell superconductor-semiconductor nanowire qubit, Phys. Rev. B **108**, L121406 (2023).

[28] W. A. Little and R. D. Parks, Observation of quantum periodicity in the transition temperature of a superconducting cylinder, Phys. Rev. Lett. **9**, 9 (1962).

[29] Y. Liu, Y. Zadorozhny, M. M. Rosario, B. Y. Rock, P. T. Carrigan, and H. Wang, Destruction of the global phase coherence in ultrathin, doubly connected superconducting cylinders, Science **294**, 2332 (2001).

[30] I. Sternfeld, E. Levy, M. Eshkol, A. Tsukernik, M. Karpovski, H. Shtrikman, A. Kretinin, and A. Palevski, Magnetoresistance oscillations of superconducting al-film cylinders covering InAs nanowires below the quantum critical point, Phys. Rev. Lett. **107**, 037001 (2011).

[31] G. Schwiete and Y. Oreg, Persistent current in small superconducting rings, Phys. Rev. Lett. **103**, 037001 (2009).

[32] S. Vaitiekėnas, P. Krogstrup, and C. M. Marcus, Anomalous metallic phase in tunable destructive superconductors, Phys. Rev. B **101**, 060507(R) (2020).

[33] G. Giavaras and R. Aguado, Flux-tunable supercurrent in full-shell nanowire Josephson junctions, Phys. Rev. B **109**, 024509 (2024).

[34] P. Sriram, S. S. Kalantre, K. Gharavi, J. Baugh, and B. Muralidharan, Supercurrent interference in semiconductor nanowire Josephson junctions, Phys. Rev. B **100**, 155431 (2019).

[35] C. Payá, R. Aguado, P. San-Jose, and E. Prada, Josephson effect and critical currents in trivial and topological full-shell hybrid nanowires, Phys. Rev. B **111**, 235420 (2025).

[36] C. W. J. Beenakker, Universal limit of critical-current fluctuations in mesoscopic Josephson junctions, Phys. Rev. Lett. **67**, 3836 (1991).

[37] P. Krantz, M. Kjaergaard, F. Yan, T. P. Orlando, S. Gustavsson, and W. D. Oliver, A quantum engineer's guide to superconducting qubits, Appl. Phys. Rev. **6**, 021318 (2019).

[38] J. Koch, T. M. Yu, J. Gambetta, A. A. Houck, D. I. Schuster, J. Majer, A. Blais, M. H. Devoret, S. M. Girvin, and R. J. Schoelkopf, Charge-insensitive qubit design derived from the Cooper pair box, Phys. Rev. A **76**, 042319 (2007).

[39] G. Catelani, R. J. Schoelkopf, M. H. Devoret, and L. I. Glazman, Relaxation and frequency shifts induced by quasiparticles in superconducting qubits, Phys. Rev. B **84**, 064517 (2011).

[40] P. Groszkowski, A. D. Paolo, A. L. Grimsmo, A. Blais, D. I. Schuster, A. A. Houck, and J. Koch, Coherence properties of the 0-π qubit, New J. Phys. **20**, 043053 (2018).

[41] M. Valentini, M. Borovkov, E. Prada, S. Martí-Sánchez, M. Botifoll, A. Hofmann, J. Arbiol, R. Aguado, P. San-Jose, and G. Katsaros, Majorana-like Coulomb spectroscopy in the absence of zero-bias peaks, Nature (London) **612**, 442 (2022).

[42] G. de Lange, B. van Heck, A. Bruno, D. J. van Woerkom, A. Geresdi, S. R. Plissard, E. P. A. M. Bakkers, A. R. Akhmerov, and L. DiCarlo, Realization of microwave quantum circuits using hybrid superconducting-semiconducting nanowire Josephson elements, Phys. Rev. Lett. **115**, 127002 (2015).

[43] A. Danilenko, D. Sabonis, G. W. Winkler, O. Erlandsson, P. Krogstrup, and C. M. Marcus, Few-mode to mesoscopic junctions in gatemon qubits, Phys. Rev. B **108**, L020505 (2023).

[44] S. Skalski, O. Betbeder-Matibet, and P. R. Weiss, Properties of superconducting alloys containing paramagnetic impurities, Phys. Rev. **136**, A1500 (1964).

[45] F. Peñaranda, R. Aguado, P. San-Jose, and E. Prada, Even-odd effect and Majorana states in full-shell nanowires, Phys. Rev. Res. **2**, 023171 (2020).

[46] C. Payá, S. D. Escribano, A. Vezzosi, F. Peñaranda, R. Aguado, P. San-Jose, and E. Prada, Phenomenology of Majorana zero modes in full-shell hybrid nanowires, Phys. Rev. B **109**, 115428 (2024).

[47] C. Payá, P. San-Jose, C. J. S. Martínez, R. Aguado, and E. Prada, Absence of Majorana oscillations in finite-length full-shell hybrid nanowires, Phys. Rev. B **110**, 115417 (2024).

[48] P. San-Jose, C. Payá, C. M. Marcus, S. Vaitiekėnas, and E. Prada, Theory of Caroli–de Gennes–Matricon analogs in full-shell hybrid nanowires, Phys. Rev. B **107**, 155423 (2023).